

June 2004 Update to the NOvA (P-929) Proposal

Appendix B. Totally Active Scintillator Detector (TASD)

B.1. Overview

A totally active liquid scintillator detector holds the promise of being able to produce better physics for the same amount of money as the baseline detector described in Chapter 7 of the March 15, 2004 NOvA Proposal. During the last several months we have made significant progress in understanding many of the issues relevant to this question in the areas of simulations, methods of construction, installation and cost. This proposal appendix reports the progress achieved to date in these areas. Even though it is premature at this time to reach definite conclusions regarding the relative merit of the two approaches, we are strongly encouraged by the results so far.

The TASD detector that has been considered so far has a total mass of 25,000 metric tons (25 kT), half that of the baseline detector. Like the baseline detector, TASD is a tracking calorimeter with alternating vertical and horizontal planes of active liquid scintillator contained in PVC extrusions, as shown in Figure B.1. Unlike the baseline detector there is no passive absorber, so TASD is 85% active liquid scintillator and 15% PVC. Each of 1845 planes in the detector is made from 14 extrusions, each 17.5 m long and 1.28 m wide. The 1.28 m width is composed of 32 cells, each 3.9 cm wide transverse to the beam directions and 4.5 cm deep along the beam direction. There are 1 mm thick internal PVC walls between the cells in each extrusion and 2 mm thick external PVC walls. A looped 0.8 mm diameter waveshifting fiber in each cell routes light to an APD readout, with both ends of the fiber feeding the same APD pixel. The APDs and their readout are identical to the baseline detector readout described in Chapter 7 of the NOvA Proposal. The detector readouts are located on the top and on one side of the 17.5 m by 17.5 m device. These parameters are similar but somewhat different than for the baseline detector, the differences being the first attempt to optimize for a rather different kind of a detector.

Mass	25 kT
Width	17.5 m
Height	17.5 m
Length	90.4 m
Number of Layers	1845
Mass of PVC extrusions	3.85 kT
Mass of Liquid Scintillator	21.15 kT
% of detector which is active	85 %

Table B.1: Totally Active Scintillator Detector (TASD) Parameters.

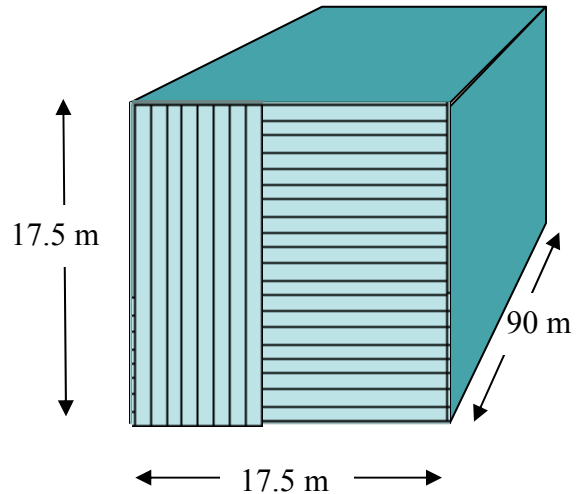


Figure B.1: TASD is composed of 17.5 meter long PVC extrusions filled with liquid scintillator. Each successive layer of the detector has alternating horizontal and vertical cells.

B.2. Detector Design

B.2.1. Overview: The parameters of the TASD active elements are listed in Table B.2. Compared to the NOvA baseline detector, the extrusions are wider (32 cells to match the APD 16-channel unit vs. 30 cells) and the cells themselves are deeper along the beam direction to give more light (4.5 cm in TASD vs. 2.56 cm in the baseline). Com-

pared to the NOvA baseline detector, the extrusions are longer, 17.5 m vs. 14.6 m. The cell thickness and the cell length are such that the light reaching the APD from the far end of the cell is the same in T ASD as for the baseline.

Extrusions	Polyvinyl Chloride (PVC) with 10-15% TiO ₂ for reflectivity
Extrusion Length	17.5 m
Extrusion Width	1.28 m
Extrusion Thickness	4.9 cm
Cells per Extrusion	32
Extrusion Outer Wall Thickness	2.0 mm
Extrusion Inter-Cell Wall Thickness	1.0 mm
Density of PVC	1.3 g/cc
Extrusion Mass (Empty)	149 kg
Cell Width (inside dimension)	3.9 cm
Cell Thickness (inside dimension)	4.5 cm
Cell Volume	0.030 m ³
Extrusions in the Detector	25,830
PVC Mass in the Detector	3,850 metric tons
Liquid Scintillator	Bicron BC517L
Density of Liquid Scintillator	0.860 g/cc
Liquid Scintillator Mass (per cell)	25.6 kg
Liquid Scintillator Mass (per extrusion)	819 kg
Extrusion Mass (Full)	968 kg
Cells Per Plane	448
Number of Cells in the Detector	826,560
Liquid Scintillator Mass in the Detector	21,150 metric tons
Wavelength Shifting Fiber (WLS)	Kuraray
WLS Diameter	0.8 mm
WLS Length Per Cell	35 m
WLS Length for the Detector	30,583 km
WLS Volume in the Detector	15.4 m ³
WLS Mass in the Detector	15.9 metric tons

Table B.2: T ASD Element Parameters

The PVC material, Liquid Scintillator, Wavelength-Shifting (WLS) fiber, Avalanche Photodiodes (APD), and Data Acquisition used in T ASD are identical to that described in Chapter 7, Sections 4, 5, and 6 of the NOvA proposal.

B.3. Structural Considerations

B.3.1. Overview: In the baseline design an 8-inch thick lamination of particleboard easily provides the structure to hold its own mass and the additional 19% more mass in the form of a 1-inch thick PVC extrusion loaded with liquid scintillator. The function of the PVC extrusion is to hold the liquid in a specific shape. In T ASD the extrusions must do both jobs: contain the liquid and provide the strength to hold up a 25 kT structure.

The elastic modulus of particleboard and PVC are very similar, with both around 0.4×10^6 psi. In the case of the baseline detector made of 15 m tall particleboard, the loads are within structural safety margins as might be expected for a wood structure about 4 or 5 stories (48 ft) tall. For the T ASD design, it is clear that we need to understand the details of a structure 17.5 m high (5 or 6 stories, 57 ft high) made from PVC with no part thicker than 2 mm. This would be a unique structure and is by no means a standard application of building materials.

The following sections are an attempt to analyze this structure in simple steps to give the reader some confidence that the composite structure can support the 25 kT load. The work described below is fairly new and will require more checking. We believe it will be prudent to test mock-up sample portions of this structure to destruction to verify the engineering calculations.

B.3.2. Structural Analysis of a Single Vertical Cell:

A simple finite element analysis of a single vertical cell against the hydrostatic pressure of the contained liquid in a 17.5 m high cell indicates that a cell with 2 mm thick PVC walls can just contain the hydrostatic pressure of the liquid column with a safety factor of 1.09, see Figure B.2. Common engineering practice allows structures that use up to 67% of the yield of the material – this would correspond to a safety factor of 1.5, so we are short of the standard requirement.

Adding a ~3 mm radius chamfer at the corner of the cell increases its strength to a safety factor of 1.55, which is encouraging (see Figure B.3). Such a chamfer also alleviates the loss of light which can occur if the WLS fiber lands in the corner of the cell. See the NOvA proposal, Figure 7.11.

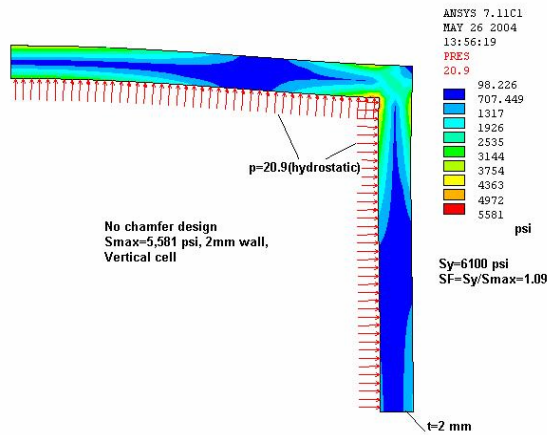


Figure B.2. Finite element analysis of a single vertical cell. The pressure at the bottom of the cell is 20.9 psi due to the 17.5m of liquid in the cell.

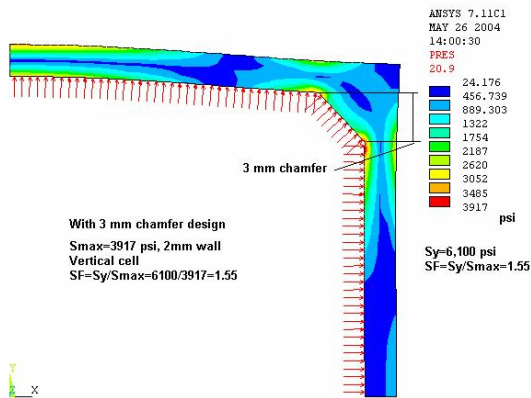


Figure B.3. Finite element analysis of a single vertical cell with a chamfered corner.

B.3.3. Structural Analysis of Horizontal Cells:

We now examine the stresses within a set of 32 horizontal cells in one horizontal extrusion module. The liquid in these cells is a connected mass via the manifold which allows filling and WLS fiber routing. When filled with liquid, the thin 1 mm cell dividers in the module are in tension and just keep the side walls from bowing outwards. As shown in Figure B.4, the pressure in the cells rises from 0.0 psi in the top cell to 1.49 psi in the bottom cell as the weight of the liquid above accumulates. This pressure is small compared to the vertical cell case just analyzed in the previous section, since the column of liquid contained is only one-fourteenth as large.

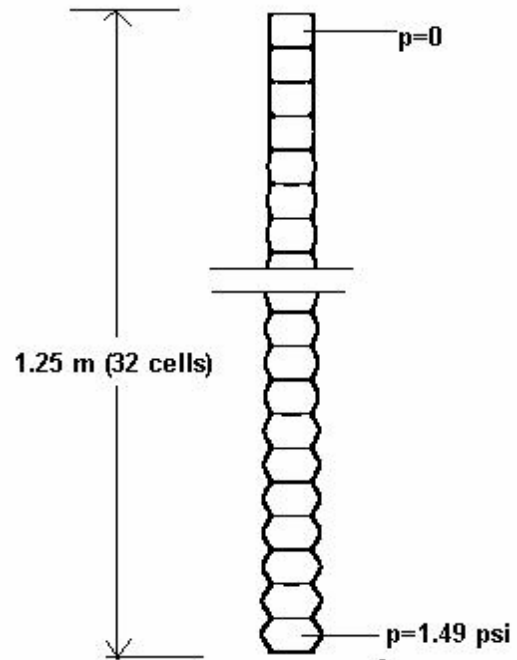


Figure B.4. A cross-section of the cells in a horizontal extrusion.

Next we consider two 1.28 m wide extrusions stacked horizontally on top of each other. Now we have a thick membrane between the extrusions with two 2 mm walls forming a 4 mm stiff beam as shown in Figure B.5.

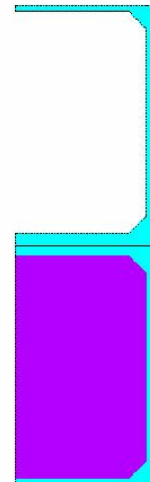
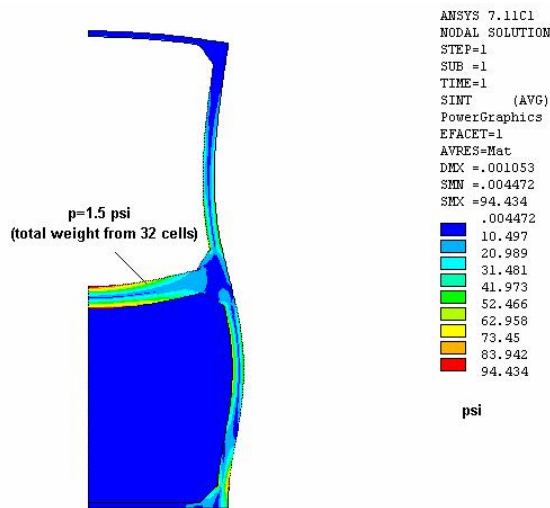


Figure B.5. Diagram of the interface between two stacked extrusions. Think of this as a “half-ladder” diagram with a stiff 4 mm thick rung passing the loads laterally to the 2 mm thick side walls of the extrusion.

A finite element analysis finds that the maximum stress in the 4 mm beam is only 94 psi as shown in Figure B.6. This analysis assumes the two 2 mm beams are bonded together. If there is no bonding and the two beams just sit on top of one another, the stress will double for each beam.



For the case where the load transfer from one module to another one

Figure B.6. Finite Element analysis of the interface between two stacked extrusions.

One more calculation is required to understand the horizontal extrusions under load. The vertical side walls will suffer from a buckling stress as the load above the bottom cell attempts to pancake that cell. We remind the reader that we are still calculating a worst case here and taking no credit for the adjacent vertical cells in the detector. In this case the engineering rule of thumb is that a safety factor of 3 is required against such buckling collapse.

Figure B.7 shows the result of the finite element analysis of the PVC cell assuming all the top load transfer is through the side wall. The load from the 14 filled and stacked extrusions is 22.3 pounds of force per inch. The 1.5 psi hydrostatic pressure from the liquid inside that one bottom cell of the bottom extrusion is also included. The calculated safety factor is 3.3.

Finally, having determined that the bottom horizontal cell will not buckle, Figure B.8 shows the finite element stress plot for the same cell. This is the calculated actual working stress for the walls and the result is well within the limits of the PVC material.

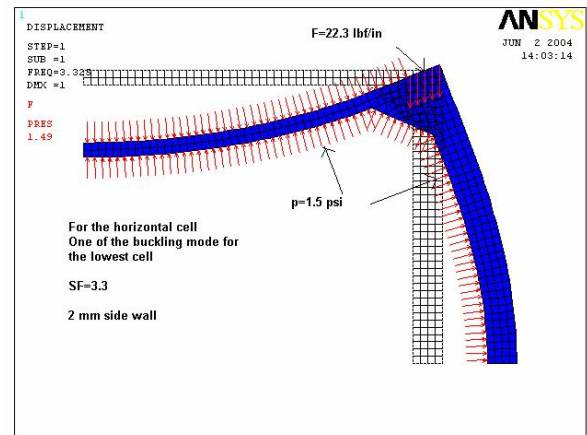


Figure B.7. Lowest cell buckling calculation assuming all the top load transfer is through the side wall.

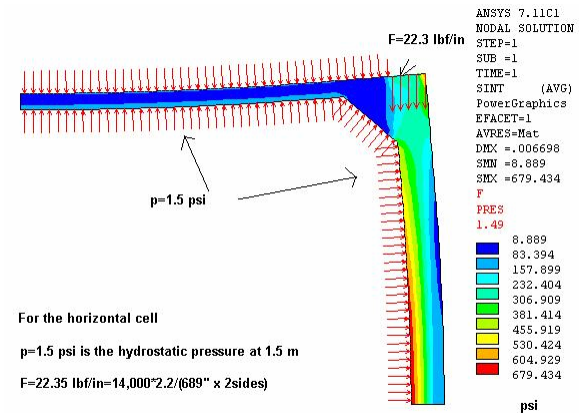


Figure B.8. Calculated working stress in the bottom horizontal cell.

B.3.4. Composite Structural Analysis:

The simplified cases discussed in the previous two sections do not take into account the fact that every vertical cell is trapped by supporting horizontal cell walls spaced every 4 cm. Similarly every horizontal cell exterior wall is adjacent to a 2 mm thick vertical cell wall and is trapped by vertical cells with interior walls spaced every 4 cm. These exterior cell walls in the adjacent extrusion plane act as buttresses against the forces

seen by the central extrusion. Only the first and last walls of the detector will not see the buttress effect. This is illustrated in Figure B.9.

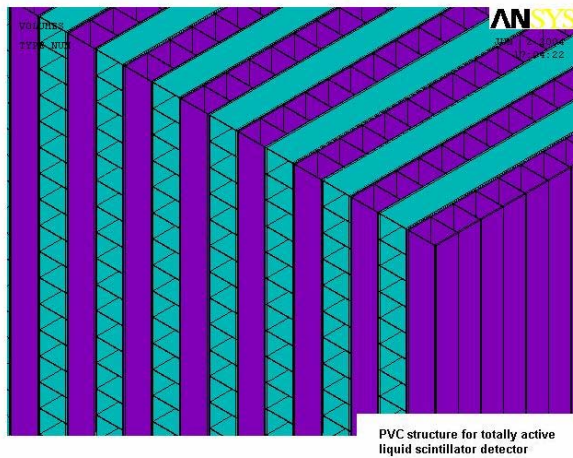


Figure B.9. Detail of the PVC cell structure in the alternating vertical and horizontal extrusions.

The composite structure with bonded laminations of vertical and horizontal extrusion cells should be much stronger than any single cell in isolation. A preliminary finite element analysis of this composite structure assuming perfect bonding between the layers indicates that this structure should have a very high safety factor greater than 20. The analysis indicates a maximum stress in the PVC of only about 1000 psi. We need to check all these calculations and we will need to test sample structures to verify the calculations.

B.4. Detector Construction

B.4.1. Module Factories: The multi-cell PVC modules will be purchased as units from commercial extruders and shipped directly to three assembly factories, likely located at collaborating institutions. The assembly factories install the end-cap seal on each extruded module, install the looped WLS fiber in each cell of the module, and route the fiber ends through a manifold that both seals the second end of the extrusion and directs the fibers to an optical connector. The factories will leak test each extrusion before shipping to the far site. To complete the modules during 4 years (200 working days per year) of construction, each factory must complete 12 modules per day with a crew of 4 technicians. This is the same module

construction rate we assumed in the baseline even though the T ASD modules are a little longer and have 32 instead of 30 cells.

B.4.2. Installation at the Far Site: Compared to the baseline detector, T ASD has half the mass and so construction at the Far Site handles half as much material. In fact the baseline design has 144,000 pieces (PVC extrusions and sheets of particle board), while T ASD has only 25,830 extrusions to handle. Therefore installation of the T ASD Far detector can be completed in half the time with a smaller size installation crew than assumed in the baseline design. We could install this detector in only 2 years. This is an advantage because the four year long factory assembly line can begin in parallel with the Far Detector Building construction during the first part of the construction project.

B.4.3. Assembly Procedure: We have examined two modes of construction at the Far Site. In the first, we minimize the movement of material by lifting a completed PVC extrusion module directly from its shipping crate to the final position on the face of the detector. Each 149 kg module would be “glued” in place such that an installation pace of 35 extrusion modules per shift could be maintained. This rate installs 5 full planes per day during two shifts. We use the word “glue” above to cover various possible techniques including actual glues, ultrasonic welding, or PVC welding using heat plus sticks of additional PVC material.

An alternate mode of construction would assemble super-planes of detectors on the floor of the building. We imagine assembling 10 – 20 planes of the detector in this horizontal mode, creating a super-plane that is 0.5 – 1.0 meter thick and 17.5 m by 17.5 m on a side. At 2.1 metric tons per single PVC plane, this empty super-plane structure would weigh 21 – 42 tons and be raised into position by a strong-back in a construction technique much like that used for the 8 m diameter MINOS Far Detector planes as shown in Figures B.10 and B.11. This technique makes the gluing of adjacent planes simpler (gravity assists to hold the modules in place) with the complication of raising the larger assemblies and attaching them to the growing empty detector mass.



Figure B.10. Assembly of a MINOS plane on the floor of the detector hall.



Figure B.11. Raising a MINOS plane using a strong-back.

B.4.4. Filling the Detector with Liquid Scintillator:

In the baseline design 2 shifts with 2 person crews are adequate to fill the detector with liquid scintillator at 5 gallons per minute. This is the same rate used in filling MACRO. In the TASD design, 3 times as much liquid must be pumped into place in half the time. A rate of 15 gallons per minute seems attainable, but we still need twice as many

people per shift compared to the baseline design and this is in our cost estimate.

The higher rate of liquid consumption during construction also has implications for mixing the mineral oil with pseudocumene at the far site because larger storage tanks and multiple mixing systems would be required. Instead of mixing on site, we are investigating vendors to do the mixing at their plants before shipping the mineral oil north from Texas. We would still keep a 2 week buffer of mixed product at the far site and that would require about the same number of storage tanks as in the baseline detector.

The quality assurance testing effort at the far site would also be larger and need to keep up with the incoming shipments. Sufficient storage capacity would have to exist such that mixed loads failing our QA procedure could be rejected without schedule impact.

B.5. TASD ES&H Considerations

The ES&H issues for the TASD design are similar to the baseline design as discussed in Chapter 7, Section 7 of the NOvA proposal. The ES&H concerns for the flammability of the absorber disappear, but similar concerns and environmental concerns for the liquid scintillator increase as the mass of the liquid scintillator increases from 6.9 kT to 21.2 kT. We will likely have to design increased secondary containment systems for this increased mass of liquid scintillator.

B.6. Simulations of Detector Performance

The simulations of this detector for the $\nu_\mu \rightarrow \nu_e$ appearance channel are somewhat more sophisticated and complex than for the baseline so as to take advantage of the more extensive information available. They naturally divide into several sequential parts:

- a) Generation of the event interaction.
- b) Calculation of the detector response to the generated tracks.
- c) Reconstruction, i.e. track finding and fitting. For more than 1 hit in a plane, the fit uses mean of cell positions weighed by pulse height.
- d) Calculation of various parameters associated with each track.

- e) Assignment of particle identity to each track (e, μ , p, γ or neither).
- f) Calculation of interaction vertex and angles of γ 's with respect to the electron
- g) Preliminary identification of events with the right measured energy and with potential electron candidates in both planes and no μ 's or γ 's (compatible with making a π^0 with the electron)
- h) Optimization of signal/background separation using maximum likelihood method

For the oscillation parameters and the total rates we have used:

- a) Current best estimates for atmospheric parameters, i.e. $\Delta m^2_{23} = 2.5 \times 10^{-3} \text{ eV}^2$ and $\sin^2 \theta_{23} = 1$.
- b) $P(\nu_\mu \rightarrow \nu_e) = 0.05$, i.e. somewhat below the CHOOZ limit.
- c) Source to detector distance of 810 km.
- d) Detector at 12 km transversely from the beam line.
- e) Total exposure of 125 kT yrs (before fiducial volume cuts) with 3.7×10^{20} protons per year.
- f) The NuMI medium energy beam configuration.

B.7. Detector Performance

We address next the issue of detector performance, emphasizing those features that are most relevant for the physics of highest current interest.

B.7.1. Energy resolution: There are several areas where energy resolution helps in quality of physics obtained. In brief, they are:

- a) In reducing the intrinsic beam ν_e background for the $\nu_\mu \rightarrow \nu_e$ appearance analysis. This is the only handle one has on that background.
- b) In reducing the NC and ν_μ CC backgrounds for this analysis; the energy distributions from these two sources generally will not peak at the oscillation maximum and be much broader.
- c) In measuring the dominant oscillation mode parameters.

- d) In dividing the identified $\nu_\mu \rightarrow \nu_e$ into different energy bins so as to get a better handle on matter effect and hence the mass hierarchy.

For the first two, the energy resolution should be good enough so that there is no appreciable broadening in the measured energy resolution due to that reason, the eventual cut being determined by the natural spread of the beam accepted. For the last two, one wants energy resolution as good as possible.

The true and measured energy distributions for all events with reconstructed electron track are shown in Figure B.12. The additional spread in measured energy distribution due to the resolution is hardly perceptible – the RMS width changes only from 19.2% to 21.4%.

Another useful way of looking at the energy resolution is to look for correlations with the fraction of the total energy that goes into the electron, effectively the $(1-y)$ parameter of the interaction. This information is shown in Figure B.13 for all the events with a reconstructed electron, where the energy information is represented as DELE, defined as the difference between the true and measured energies divided by square root of true energy in GeV. The scatter plot of the left shows DELE as a function of $(1-y)$. Clearly as y approaches zero the number of events increases and the energy resolution improves. The middle plot shows the mean energy as function of $(1-y)$ indicating adequate weighing of hadronic and electromagnetic energy deposition. Finally, the plot on the right shows DELE distribution; the width of the fitted curve is $\pm 8.7\%$. Restricting that sample to events passing all cuts for ν_e identification, reduces this width to $\pm 6.7\%$.

B.7.2. Electron / muon separation: The electrons and muons look quite different in the T ASD detector. The electrons tend to deposit more energy per plane and are more “fuzzy”, i.e. have more hits per plane. In addition, electrons, because of their showering nature tend to have larger RMS spread of the accepted hits and also have more gaps, whereas the muon tracks are rather continuous. These are the principal parameters that distinguish

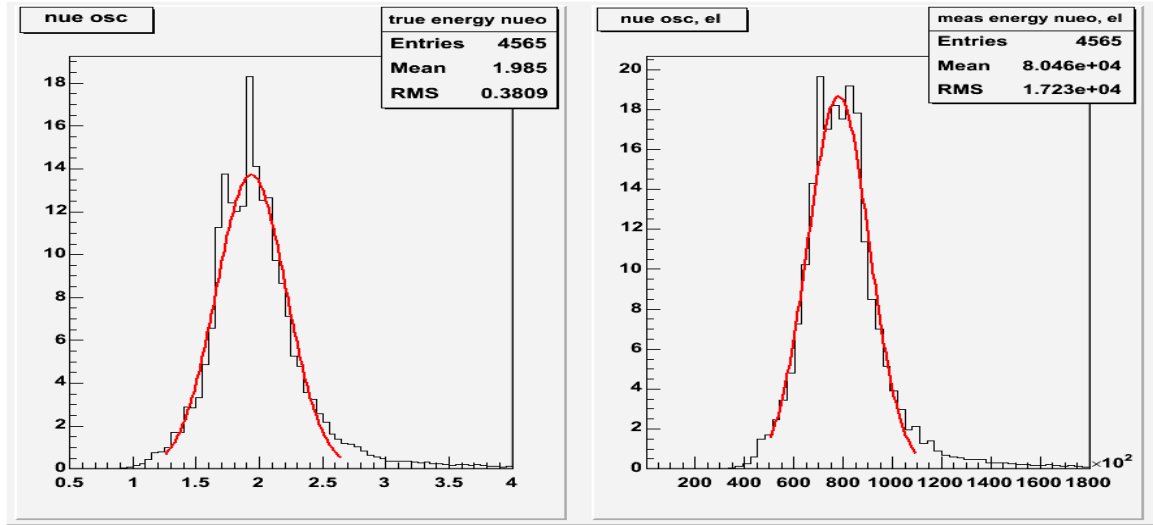


Fig.B.12. True and measured energy distributions for all events with a reconstructed electron track

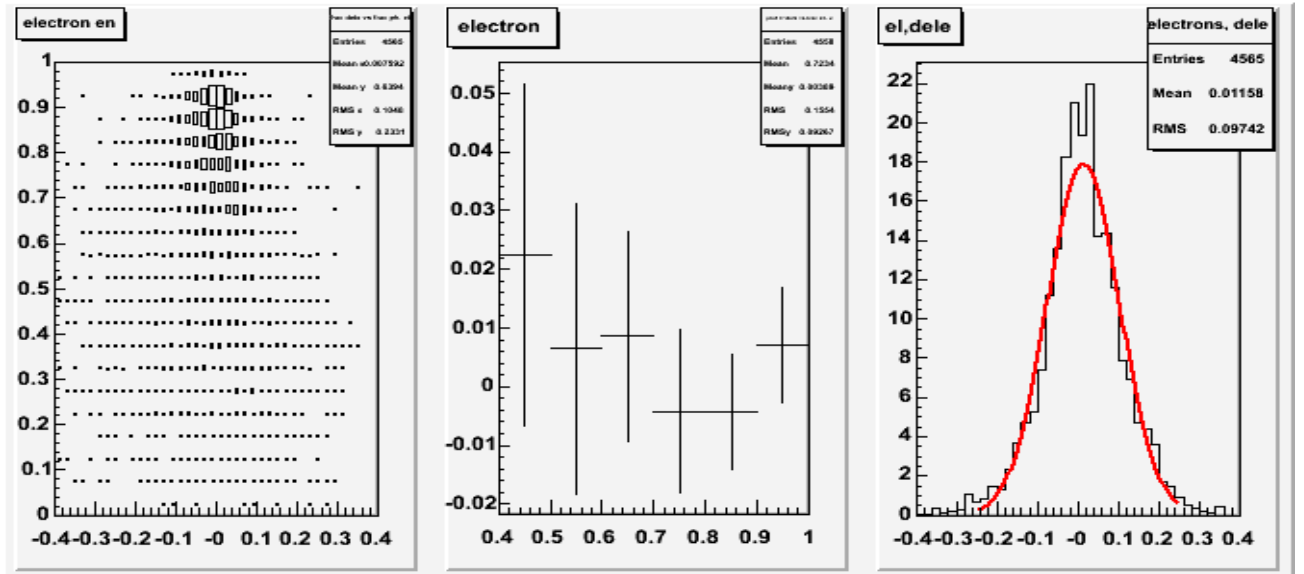


Fig.B.13. Measured – true energy difference divided by square root of true energy in GeV as function of $(1-y)$ parameter.

muons from electrons and the separation is excellent. This is illustrated in Figure B.14 where we show the first two of these parameters, i.e. average pulse height per plane and the average number of hits per plane, both for the electrons and the muons. The muon hits/per plane distribution is significantly broadened by the finite angle of the muon with respect to the beam direction, i.e. crossing of two cells in one plane. Once that is corrected the distribution will be even narrower.

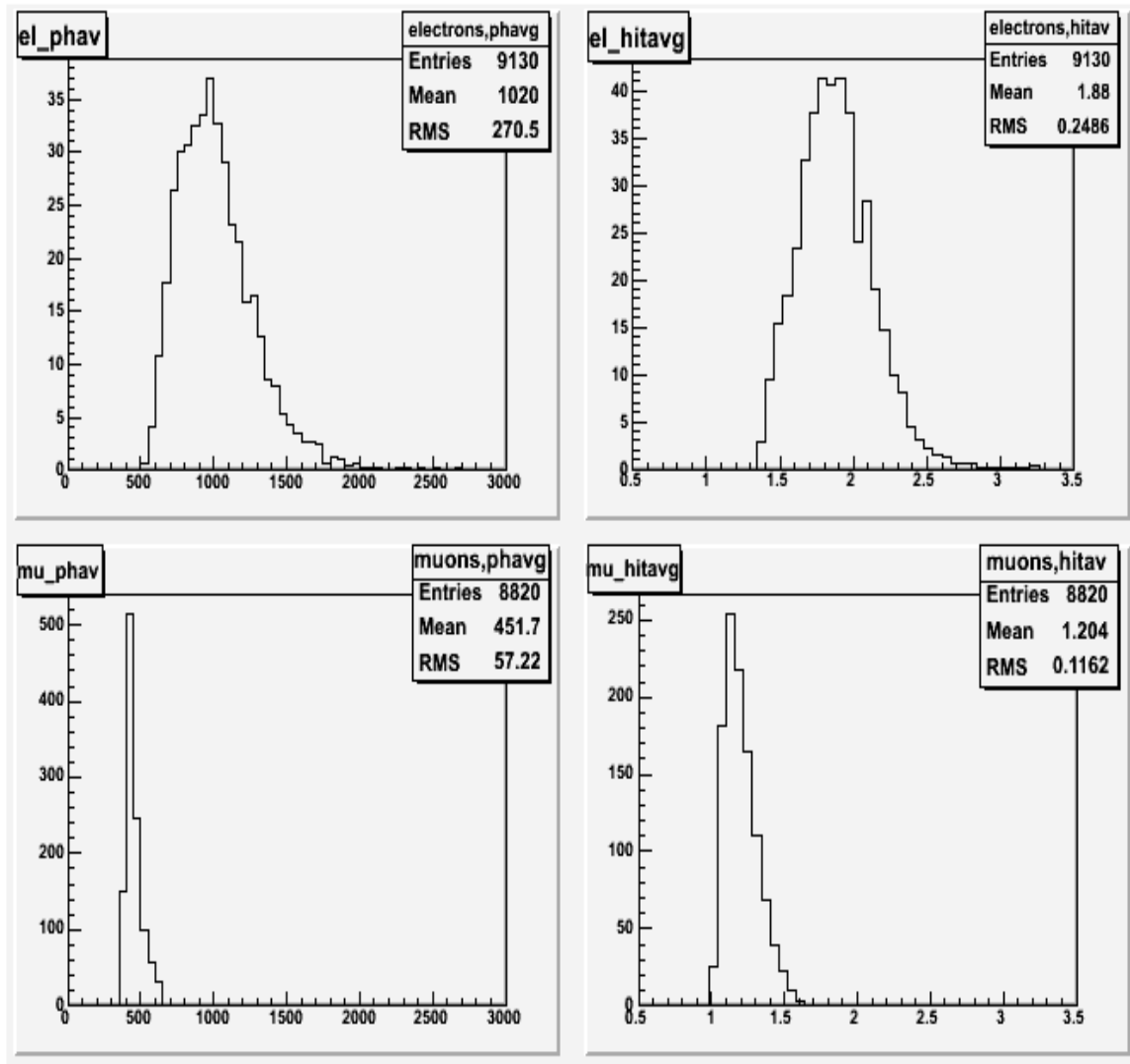


Figure B.14. Distributions of average pulse height/plane (left) and average no of hits/plane (right) for electron CC events (top) and muon CC events (bottom).

Figure B.15 also illustrates the T ASD performance in separating electrons and muons. We generated 40,000 ν_μ CC events and 40,000 ν_e CC events. General cuts were applied for fiducial volume, for events with energies clearly too high or too low to be of interest, and for events with no tracks found. We then require the ν_e events to have a found electron with an

average number of hits per plane > 1.4 , and require the ν_μ events to have a found muon with an average number pulse height per plane < 550 . The remaining events are separated into two bins by event total energy, and for each energy band the average pulse height per plane is plotted vs. the average number of hits per plane.

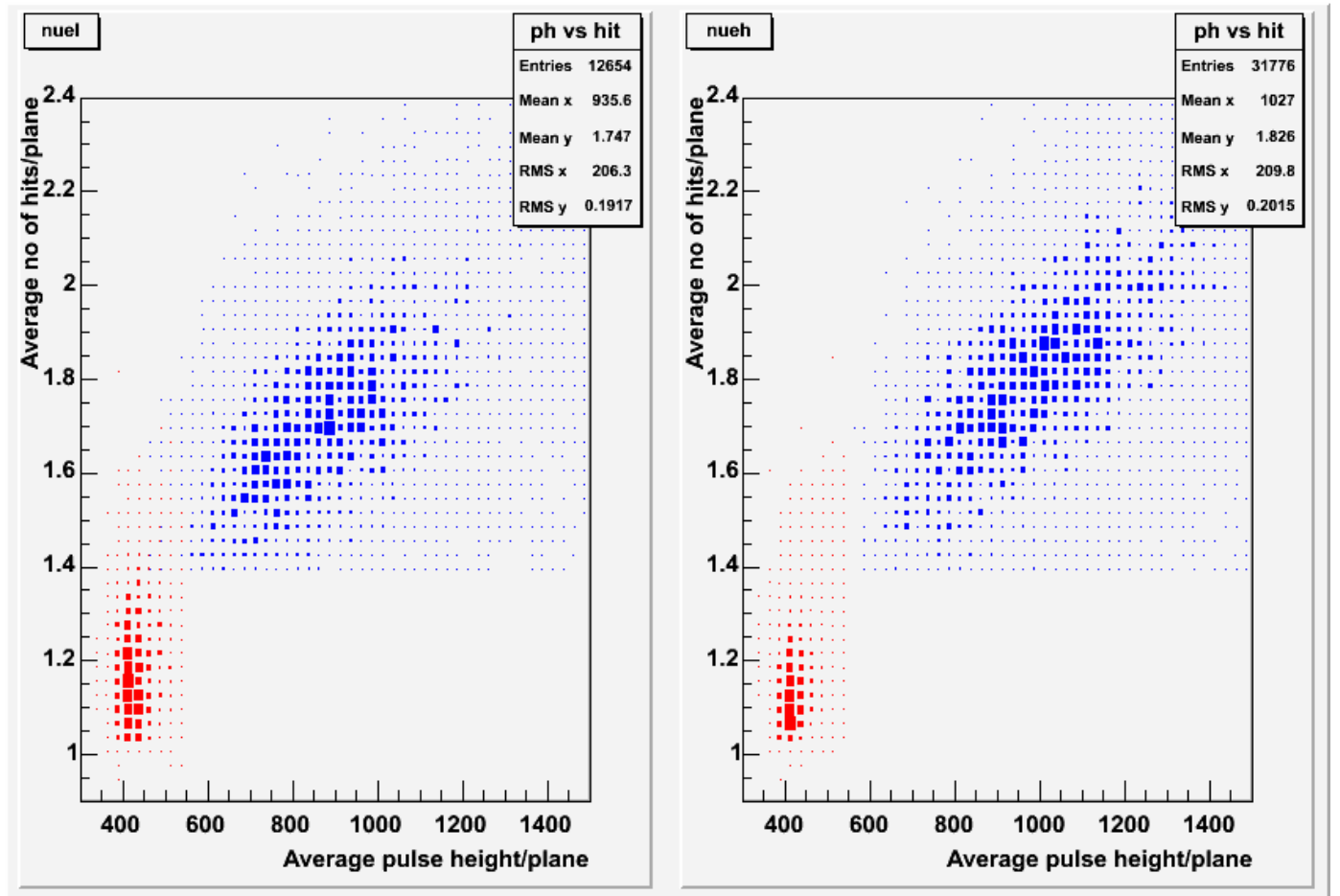


Figure B. 15. Average pulse height per plane vs. average number of hits per plane plotted for low energy events (left) and high energy events (right). Electrons are in blue, muons are in red. The “entries” in each plot are un-weighted and the higher energy events typically have rather low weights in our analyses. Thus the sum of total weights in the left and right plots are approximately equal. See text for additional details.

The above distributions, as well as other similar ones not shown here, indicate that the electron/muon separation is very clean. Thus the main mechanism for muon CC events looking like electron CC events would be production of π^0 's which then simulate electrons.

B.7.3. Acceptance: The analysis of simulations in the baseline detector requires that one keep only the events with relatively low y , i.e. effectively quasielastic, in order to keep the signal to background ratio at an acceptable level. More specifically the baseline imposes a cut of >0.7 on the fraction of total final state energy carried off by the electron.

The performance of TASD in this respect is illustrated in Figure B.16. The top figure shows the

effective $(1-y)$ distribution for all ν_e events with a reconstructed electron in both views; the middle one for that subset which passes the overall acceptance criteria (discussed below) and the bottom one for the accepted NC and ν_μ CC background events. The distribution falls off slightly near unity because even if an electron takes all the energy, generally some of it will not be included in the road used for assignment of hits to a given track. The efficiency of acceptance is very high for $(1-y) > 0.7$, but is still non zero down to a value of 0.5. One of the goals of additional work on the improvement of analysis is to extend this reconstruction and acceptance region without introducing proportionately more background.

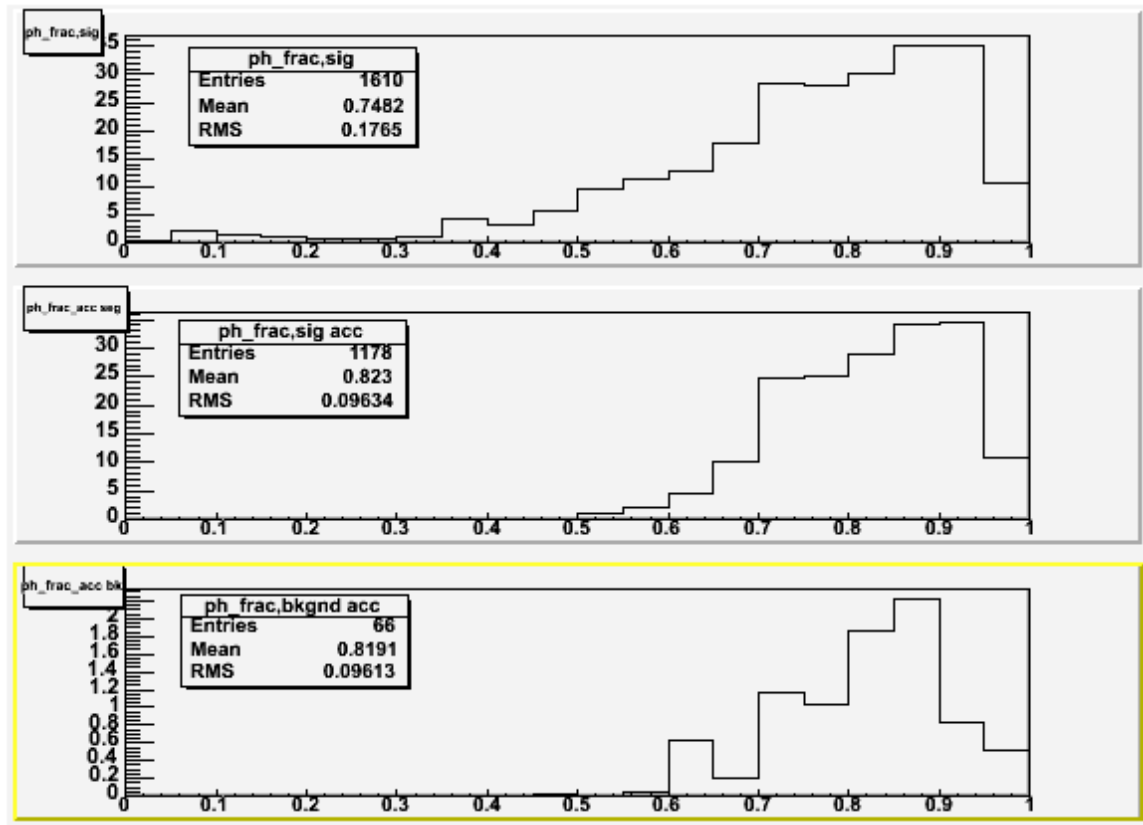


Figure B.16. Number of events as a function of fraction of total observed energy assigned to the electron track. All ν_e CC events with a reconstructed electron (top); accepted signal events (middle) and accepted background events (bottom).

B.8. Typical Events

We present a few typical events that illustrate the performance of the detector, using one example of each category of events: passing ν_e CC, failing ν_e CC, passing NC background and passing ν_μ CC background. These events really are rather typical in so far that no special effort has been made to select them. They illustrate the most important characteristics of the different categories of events: the passing ν_e events tend to be rather clean without much extraneous pulse height and with most of the energy in the electron. On the other hand the failing ν_e events have most often a low energy electron. Both NC and ν_μ CC background events tend to have an energetic π^0 that is called an electron and the muon from the ν_μ CC background events has rather low energy. In addition these background events tend to be somewhat “messier”. Each figure has the X-Z view on top and the Y-Z view on the bottom.

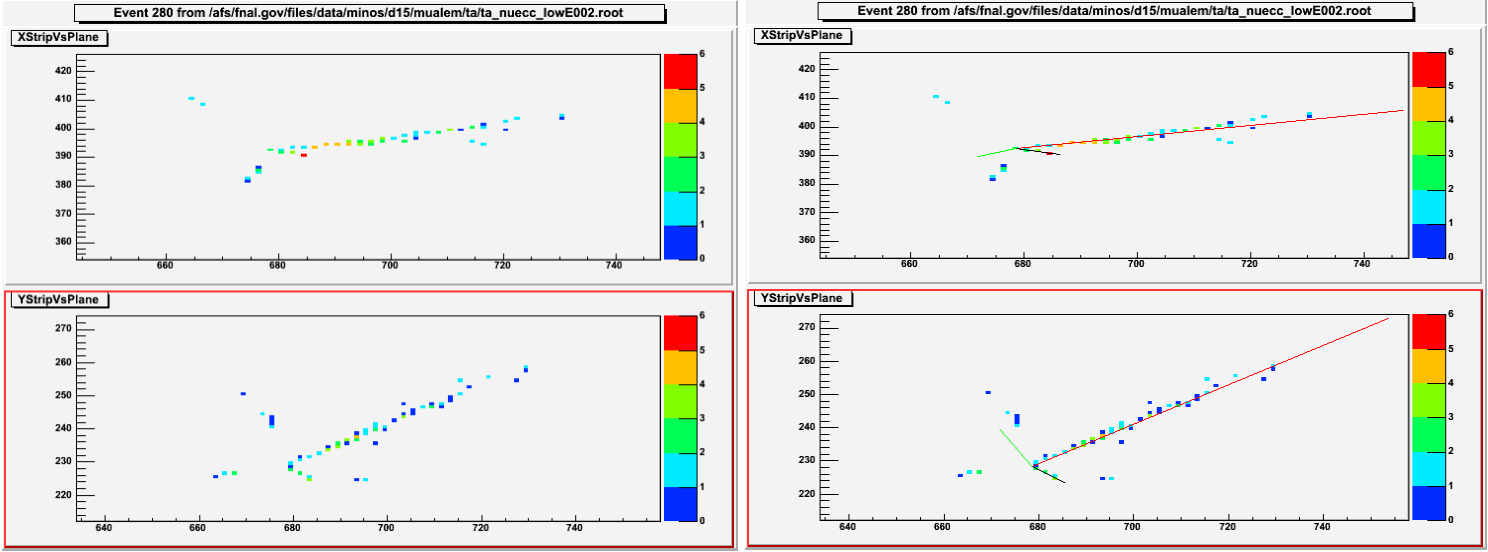


Figure B.17. Good ν_e CC event, $\nu_e + A \rightarrow p + e^- + \pi^0$, $E_\nu = 1.65$ GeV
In this figure, as well as in the ones to follow we display on the left the event using only the indicated color code to show the relative pulse height. On the right we also plot the trajectories of the final state particles: charged leptons in red, charged pions in blue, protons in black, and π^0 in green. The length of the colored trajectory is proportional to the energy of the particle but is not its expected length in the detector. The scale units are numbers of cells.

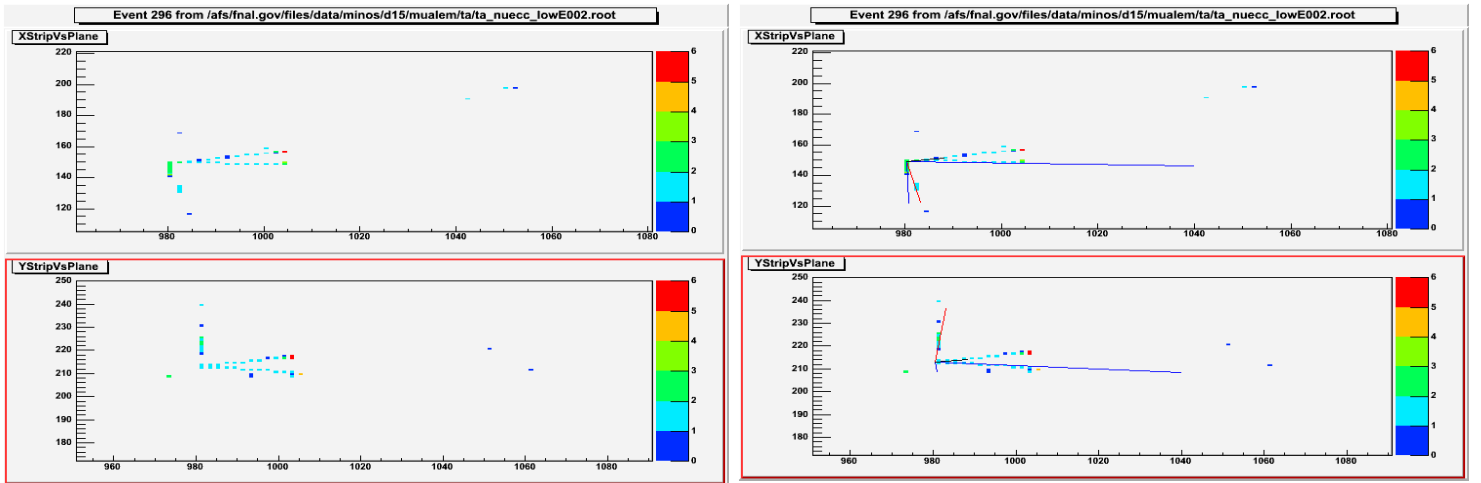


Figure B.18. A ν_e CC event which fails, $\nu_e + A \rightarrow p + e^- + \pi^+ + \pi^-$, $E_\nu = 1.87$ GeV

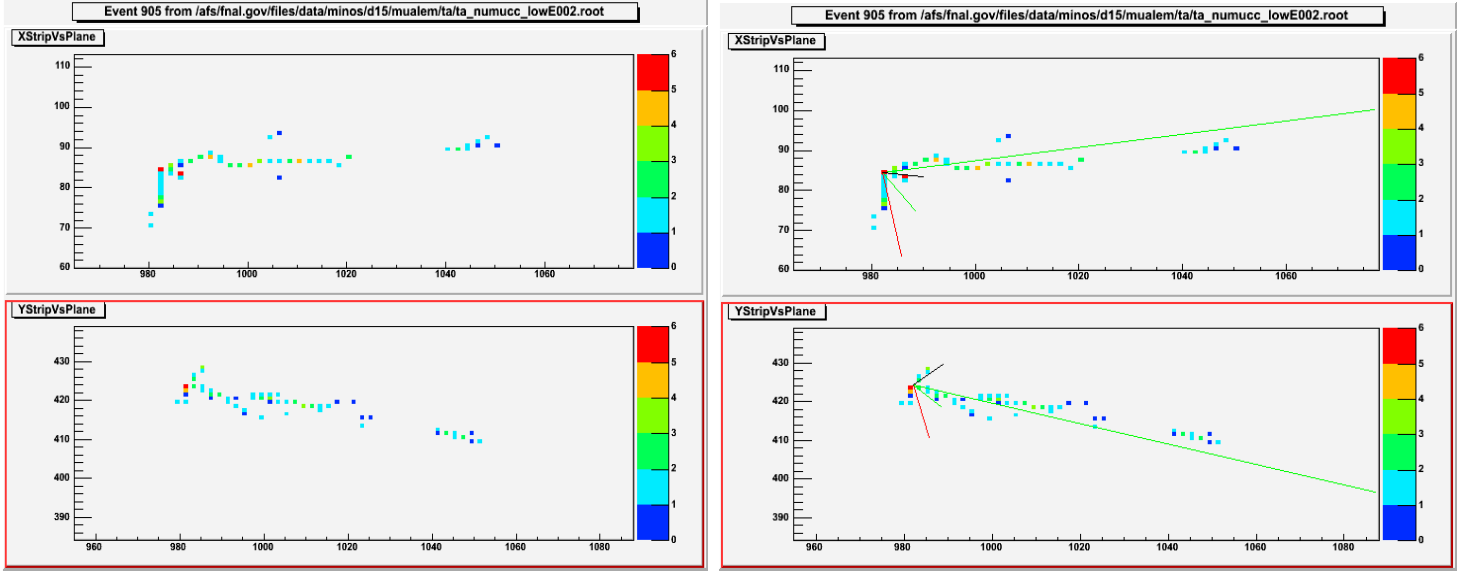


Figure B.19. A background ν_μ CC event, $\nu_\mu + A \rightarrow p + \mu^- + \pi^0 + \pi^0$, $E_\nu = 1.70$ GeV

To repeat the display code, we show on the left the event using only the indicated color code to show the relative pulse height. On the right we also plot the trajectories of the final state particles: charged leptons in red, charged pions in blue, protons in black, and neutral pions in green. The length of the colored trajectory is proportional to the energy of the particle but not to its expected length in the detector. The units are in numbers of cells.

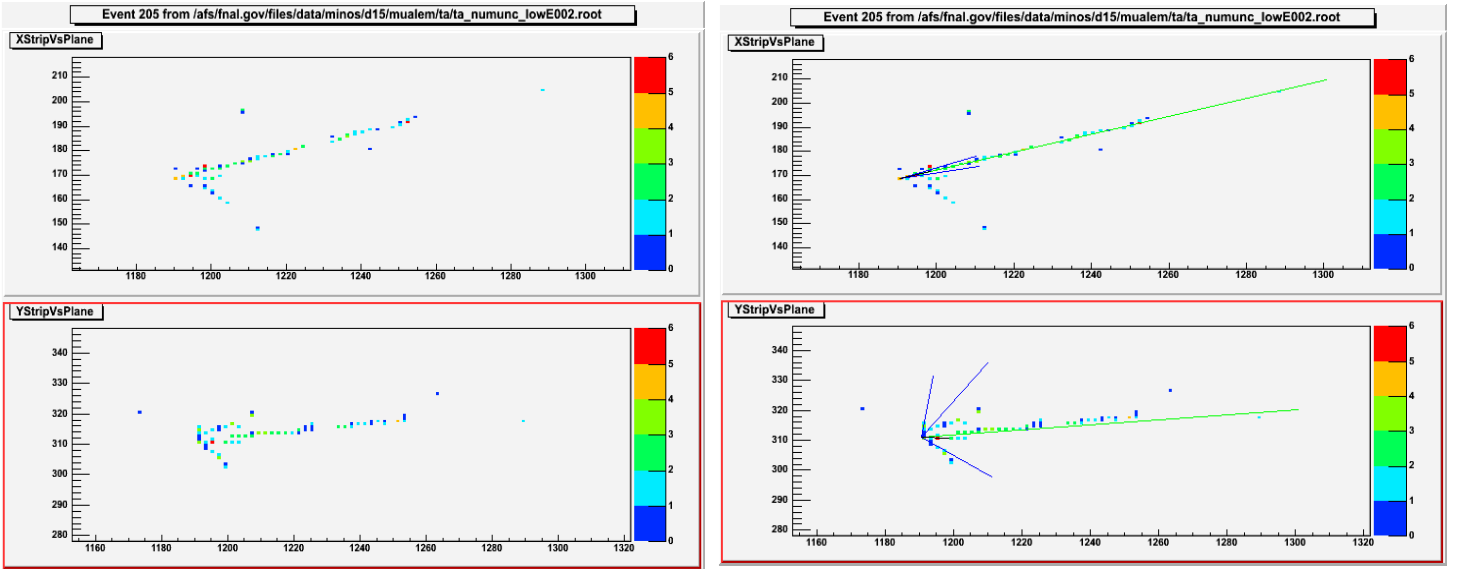


Figure B.20. A background ν NC event, $\nu + A \rightarrow p + \pi^- + \pi^- + \pi^+ + \pi^0 + \nu$, $E_\nu = 4.95$ GeV

B.9. Results of Simulations on $\nu_\mu \rightarrow \nu_e$ Appearance.

Based on the procedures described above we have obtained the first results for the sensitivity of TASD for observing $\nu_\mu \rightarrow \nu_e$ appearance. We should emphasize that the analysis used so far is still in early stages of development and undoubtedly several significant improvements in reconstruction, particle identification, and signal/background separation will be achieved in the future.

The results presented below are based on a sample of 10,000 events each of ν_e CC, ν_μ CC, NC below 6 GeV, and NC up to 20 GeV. The events were generated with uniform energy distribution and then weighted according to the expected spectrum at the detector location. The cutoff at 6 GeV was imposed since no events above that energy, with the exception of NC channel, will pass our cuts.

One can calculate the number of signal and background events as a function of a cut in the maximum likelihood ratio of the probability of an event being background or signal. For each cut value one can then calculate the figure of merit (FOM) defined as the number of signal events accepted divided by the square root of number of background events. This is equivalent to the number of standard deviations for the presence of a signal at the assumed value of $\nu_\mu \rightarrow \nu_e$ transition probability.

The results of the analysis are presented in Figure B.21 where we choose to plot the relevant values not as a function of cut parameter but rather the more meaningful number of accepted events. As one can see from the figure, at the rather broad FOM maximum one detects 90-100 events with a background of 12-15 events. Furthermore the ν_μ CC background is less than 1 event in that region. The total number of oscillated events for this exposure and these parameters is 312, before any fiducial volume or energy cuts. The TASD FOM value at maximum is 25-26, essentially the same as for the baseline detector.

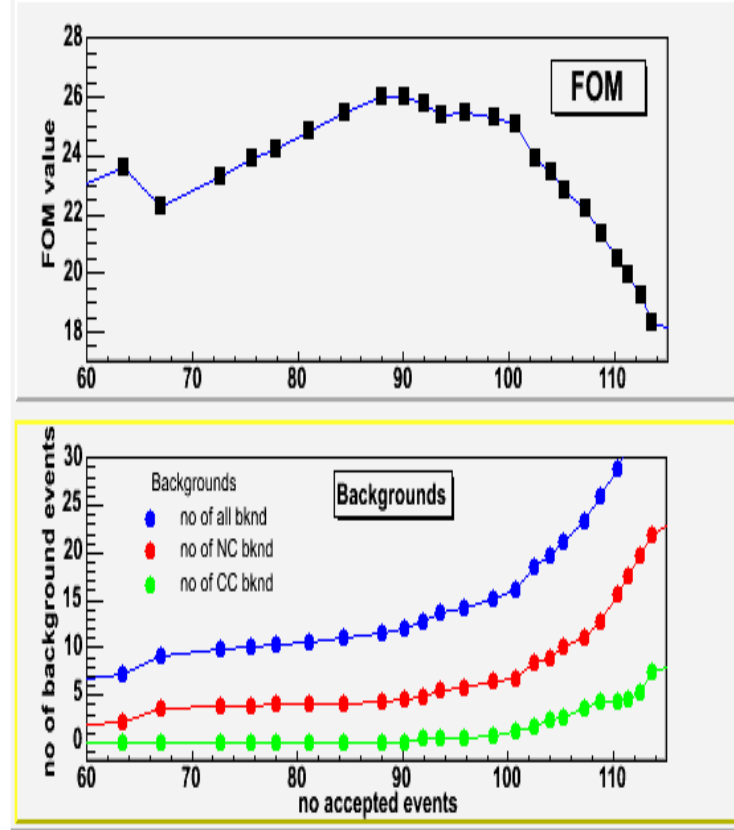


Figure B.21. Figure of Merit (FOM) and number of background events as a function of number of accepted events

Comparing TASD to the baseline detector we find that TASD has:

- Exposure = 125 kT-years
- signal = 108 events
- background = 12 -16 events
- figure of merit = 26 - 27
- oscillated ν_e efficiency = 32%

(the signal, background, and FoM are corrected here to match the assumption in Appendix D of 4×10^{20} pot/year vs. the 3.7×10^{20} pot/year assumed in the plots in this appendix.)

The baseline detector (see Appendix D of the NOvA proposal) has:

- exposure = 250 kT-years
- signal = 125 events
- background = 26 events
- figure of merit = 24.5
- oscillated ν_e efficiency = 18%

B.10. Other Physics

B.10.1. Measurement of the Dominant Mode Oscillation Parameters:

We have also performed a preliminary study of how well one could use T ASD exposure to measure the dominant oscillation mode parameters, Δm_{23}^2 and $\sin^2 2\theta_{23}$. This study was limited to the use of quasielastic ν_μ CC events and relied on a parametric representation of energy resolution without full blown reconstruction. This procedure is justified by the nature of these events which are extremely clean as is demonstrated by a typical quasielastic event displayed in Figure B.22.

The limitation on the precision of the measurement of Δm_{23}^2 and $\sin^2 2\theta_{23}$ will be statistical at some level but probably more importantly due to potential systematics. This is especially true of understanding the energy scale which is directly related to the determination of the value of Δm_{23}^2 . More specifically nuclear reabsorption of pions

produced in the primary interaction could simulate quasielastic events and shift the energy scale. We have made an attempt to estimate the size of various systematic errors and feel that the error on individual event total energy measurement can be kept at a level of 2-4% and the energy scale can be understood to better than 2%. All of the energy is visible and can be measured except for energy loss in PVC walls. That fraction can be estimated quite accurately from the trajectories.

The calculated 1-sigma and 2-sigma contour plots are displayed in Figure B.23 for a 125 kt yr exposure and assumed values of $\sin^2 2\theta_{23}$, of 0.95, 0.98 and 1.00, using a $\pm 2\%$ error on energy determination. The contour plots do not change markedly as one increases this error to 4%. It is worth noting that the precision of $\sin^2 2\theta_{23}$ improves significantly as one approaches unity; thus a possible departure from unity can be observed even if the true value of $\sin^2 2\theta_{23}$ is close to one.

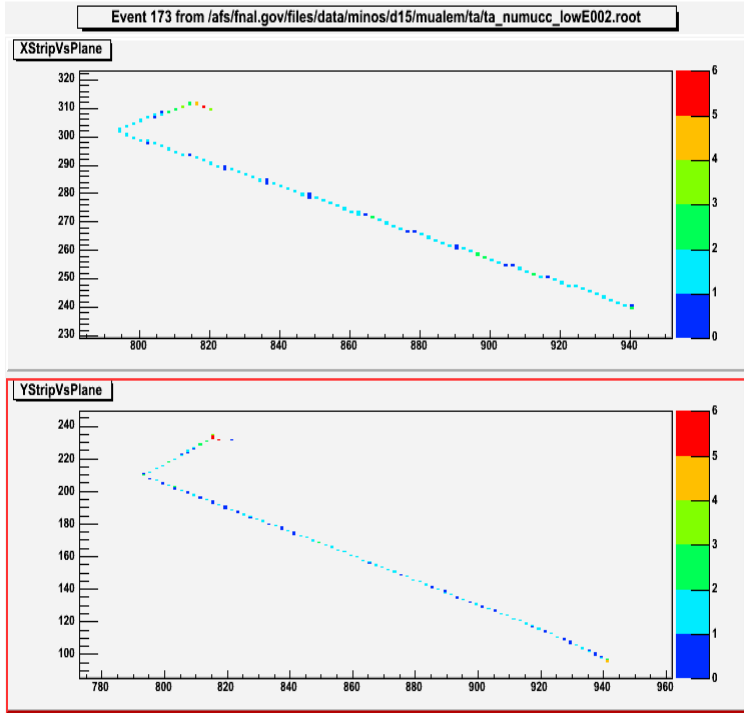


Figure B.22. An example of a quasielastic ν_μ CC interaction in the T ASD detector. Note the proton scatter near the end of its range.

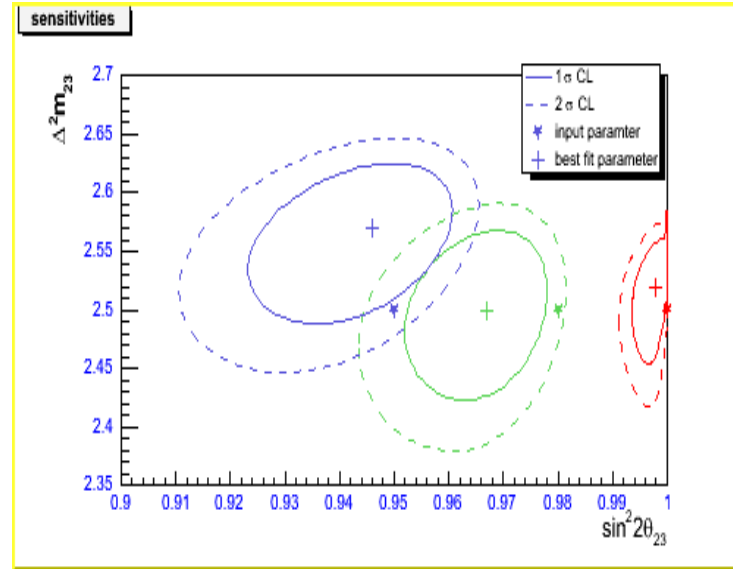


Figure B.23. 1-sigma and 2-sigma contours for simultaneous measurement of Δm_{23}^2 and $\sin^2 2\theta_{23}$ from disappearance of ν_μ CC events assuming use of only quasielastic events and a 125 kT-year exposure.

B.10.2. Matter effects:

The optimization of energy, longitudinal distance and transverse distance is somewhat different for maximum sensitivity for observing $\nu_\mu \rightarrow \nu_e$ transition and for optimum determination of the mass hierarchy. One might thus contemplate two detectors at different transverse and/or longitudinal locations, each one optimized for the different possibility.

We have investigated to what extent one can obtain sufficient spread in energy, together with adequate neutrino energy measurement, at one location with a TASD detector so as to improve matter effect sensitivity. The separation by energy is illustrated in Figure B.24. The separation cut is

made by the measured energy; and the true neutrino energy is plotted. There is clearly a significant (~ 500 MeV) and relatively non-overlapping separation between the central values of the lowest and highest energy groupings.

For the initial running, when the main limitation is due to statistics, a potential analysis based on different energy values will probably not contribute much additional information. On the other hand, looking into the future, when one might anticipate significantly higher event rates due to increases in detector mass and/or proton intensity (proton driver?), the ability to make such a separation might contribute significantly to the intrinsic physics capabilities of the experimental program.

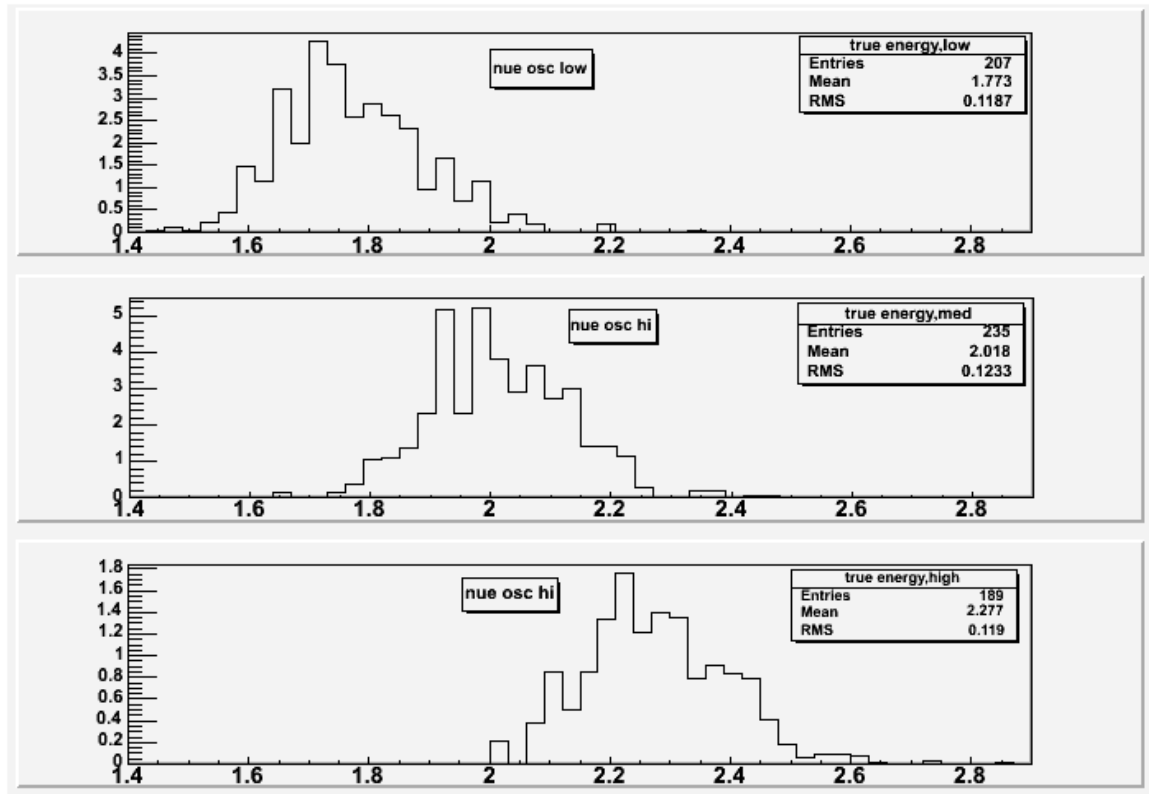


Figure B.24. The true neutrino energy spectra (in GeV) for three different sets of events grouped by the measured final state energy.

B.11. TASD Cost Estimate

We have followed the same methodology to estimate the TASD cost as that used for the baseline detector in Chapter 13 of the NOvA proposal. The results are shown in Table B.3. This cost estimate is \$ 11.8 M (about 8%) higher than the baseline detector cost estimate.

WBS	Description	Base Cost	Overhead	Contingency	Sub-total
1.0	Near Detector	3,576,039	715,208	4,291,247	8,582,494
2.0	Far Detector				
2.1	Absorber	0	0	0	0
2.2	Active Detector	63,085,322	2,259,734	18,975,965	84,321,021
2.3	FEE, Trigger and DAQ	8,335,880	835,237	5,049,761	14,220,877
2.4	Shipping&Customs Charges	4,290,330	858,066	1,072,583	6,220,979
2.5	Installation	6,050,554	1,577,944	2,884,511	10,513,009
	Detector Sub-total	81,762,086	5,530,980	27,982,819	115,275,886
3.0	Building and Outfitting				
3.1	Building	12,093,380	362,801	7,249,051	19,705,232
3.2	Outfitting	4,589,748	137,692	4,727,440	9,454,880
	Building and Outfitting Sub-total	16,683,128	500,494	11,976,491	29,160,112
4.0	Active Shield	0	0	0	0
5.0	Project Management	3,935,000	1,085,650	1,004,130	6,024,780
TPC	Total Project Cost	105,956,253	7,832,332	45,254,688	159,043,273

Table B.3: Work Breakdown Structure and second generation cost estimate for TASD.

Some of the major differences between the TASD cost and the baseline detector cost are outlined below.

B.11.1. Near Detector: The TASD Near Detector is more expensive because it has more electronics channels. We have estimated the cost of a 120 ton Near Detector with only a 3 meter long fiducial volume as a totally active detector in this cost estimate, following the philosophy of the baseline detector as described in Chapter 9, Section 9.3.2 of the proposal. In both cases a major cost driver is the use of MINOS-style PMTs and electronics instead of APDs. We are reconsidering this electronics design.

B.11.2. Absorber: There is no absorber in TASD.

B.11.3. Active Detector: TASD is more expensive because it has more scintillator, more extrusions, and more WLS fiber. We do take advantage of a quoted price break for fiber in quantities of > 20 million meters.

B.11.4. Front End Electronics: TASD has 827,000 channels vs. only 540,000 in the baseline detector.

B.11.5. Shipping Costs: TASD is cheaper because there is no absorber to ship even though there is more oil to ship.

B.11.6. Installation: TASD uses the same size installation crew but is cheaper because it can be installed in half the time, having only half the detector mass.

B.11.7. TASD Building: The TASD building is cheaper because it is narrower (73 ft vs 116 ft), only slightly taller (87 ft vs. 78 ft), and significantly shorter (377 ft vs. 642 ft) than the baseline design. This is because TASD is only 25 kT.

B.11.8. Cosmic Ray Active Shield: Unlike the baseline design, the TASD design would not have an active cosmic ray shield. Since the detector itself is 85% active, it is effectively self-shielding.

B.12. R&D for the TASD Design

There are a number of areas where additional work and/or modifications of the design of the experiment may provide a significant improvement and give a better “bang for the buck”. We enumerate some of them briefly below. A more detailed overview of NOvA R&D is presented in Appendix C.

B.12.1. Improvements in the analysis:

The analysis presented here is still somewhat primitive and less mature than for the baseline detector. Furthermore, because of significantly more information here, additional sophistication in this analysis is likely to be quite productive.

B.12.2. Optimization of hardware design:

The design used so far for the simulation is just the best guess as to what might be close to optimum. Undoubtedly, modifications slightly away from it might improve physics capabilities. Some specific areas that come to mind are:

Modifications of the cell size could be made to decrease the cost without significantly decreasing physics capabilities.

The light output could be decreased either by lower fluor concentration or by thinner wavelength shifting fibers. The design here was chosen so as to give the same light output as for the baseline detector. Because of much higher information density it is quite likely that lower light output will not degrade physics capabilities. A lower cost scintillator and/or cheaper WLS fiber cost would allow a larger detector for the same price.

The amount of inert material could be increased from the current value of approximately 15% of PVC by weight. This could be done, for example,

by making extrusions with double layers and subsequently filling one with oil and the other one with water. This way one might double the mass with very low cost penalty. Clearly such possibilities need to be investigated from the point of view of physics impact.

B.12.3. Optimization of beam design:

We have used so far the NuMI medium beam configuration as the basis for our simulations. It is quite likely that another, hybrid configuration will be much more advantageous for this physics.

B.13. Conclusions

This initial study of totally active detector configuration leads us to believe that this option may indeed be the optimum basis for the NOvA experiment. The main reasons for this point of view are:

- a) The sensitivity for the detection of $\nu_\mu \rightarrow \nu_e$ transition will very likely be somewhat better than that of the current baseline detector.
- b) A small signal should be more convincing because of relative cleanliness of the signal events.
- c) The very high suppression of the ν_μ CC background may significantly reduce the systematic error in the far detector background calculation, based on near detector measurements, since it is this background that changes most significantly between the two detectors.
- d) The measurement capability of the TASD design for the parameters of the dominant oscillation mode appears to be better than that of the baseline.
- e) Higher statistics will provide additional information, for example about the ν_e energy spectrum, which may be useful for determining the mass hierarchy.
- f) It is likely that the both the detector performance and analysis sensitivity quoted here can be significantly improved with additional studies and optimizations.